

In situ high energy synchrotron X-ray diffraction reveals the role of texture on the activation of slip and twinning during deformation of laser powder bed fusion Ti-6Al-4V

Juan Manuel Vallejos, Pere Barriobero-Vila, Joachim Gussone, Jan Haubrich, Andreas Stark, Norbert Schell, Guillermo Requena

Dr. Juan Manuel Vallejos
Instituto de Física Rosario, Bv. 27 de febrero 210 bis, 2000 Rosario, Argentina
Universidad Nacional del Nordeste, Facultad de Ingeniería, Las Heras 727, 3500 Resistencia, Argentina
Dr. Pere Barriobero-Vila, Dr. Joachim Gussone, Dr. Jan Haubrich, Prof. Guillermo Requena
Institute of Materials Research, German Aerospace Center (DLR), Linder Höhe, 51147 Cologne, Germany.
Prof. Guillermo Requena
Metallic Structures and Materials Systems for Aerospace Engineering, RWTH Aachen University, 52062 Aachen, Germany.
Dr. Andreas Stark, Dr. Norbert Schell
Helmholtz-Zentrum Geesthacht, Max-Planck-Straße 1, 21502 Geesthacht, Germany.

Keywords: high energy synchrotron X-ray diffraction, titanium alloys, twinning-induced plasticity, additive manufacturing, texture, laser powder bed fusion

The deformation behaviour of Ti-6Al-4V processed by laser powder bed fusion (LPBF) is investigated by in situ high energy synchrotron X-ray diffraction (HEXRD) during uniaxial compression. The initial microstructure of the alloy consists of a fine lamellar $\alpha + \beta$ microstructure where α lamellae are separated by thin continuous β layers within prior β grains. The anisotropy of the alloy is studied in the deformation direction using samples built at angles of 0°, 45° and 90° with respect to the LPBF base plate. The sample oriented at 0° presents higher strength-ductility trade-off compared to the conditions oriented at 45° and 90°. The in situ HEXRD experiments continuously reveal the microstructure response during deformation and that the textures for each orientation are associated with a different activation sequence of deformation mechanisms.

1. Introduction

Ti–6Al–4V is the most studied and commercially used Ti-based alloy, occupying more than half of the market share of titanium products.^[1,2] The microstructure of this alloy can be tuned by thermomechanical treatments to obtain a wide range of mechanical properties.^[3] Also, the excellent corrosion resistance that can be achieved explains the use of Ti–6Al–4V in a wide range of applications, fundamentally in aerospace and biomedical industry.^[1]

The traditional manufacturing chain used for Ti–6Al–4V comprises thermomechanical processing followed by machining.^[4] This usually leads to high machining costs and large amounts of material loss. The latter can be reduced by metal additive manufacturing (AM), which is especially attractive for decreasing the production costs of components made of Ti-based alloys.^[5] AM allows the fabrication of near net-shape metallic components with complex geometries such as load-optimized structures of minimal weight.

During laser powder bed fusion (LPBF), Ti-based alloys undergo a thermal history consisting of a steep and directional temperature gradient along the building direction. This leads to coarse and columnar prior- β grains strongly textured in the $\langle 100 \rangle_{\beta}$ orientation along the building direction.^[6-9] In addition, the high cooling rates (at the order of $10^3 \text{ }^{\circ}\text{C s}^{-1}$) produced in LPBF thermal cycles result in the $\beta \rightarrow \alpha'$ (hcp) martensitic transformation.^[6,10-14] As a consequence, a microstructure dominated by acicular α' with Burgers orientation relationship and distributed within prior β grains is usually obtained in as-built LPBF condition.

The microstructural defects that arise from LPBF (e.g. porosity), and the dominating brittle nature of α' martensite are generally considered the cause of poor ductility in as-built LPBF Ti–6Al–4V.^[15] Compared to samples with fully martensitic α' microstructure, lamellar $\alpha + \beta$ microstructures can improve the ductility in Ti–6Al–4V.^[10,12,15] To this end, decomposing the metastable α' phase into stable α and β phases has been the goal of several studies.^[6,7,9,16-18]

Opposing this, it has also been shown that a ductile mechanical response can be achieved in fully α' or dual $\alpha + \alpha'$ microstructures.^[19,20] This behaviour was attributed to a higher compatibility, i.e. slip transfer across grain boundaries, between hcp α and α' grains than in

the case of the hcp/bcc α/β interfaces. Moreover, Zheng et al. suggested that the α/β interface plays a key role in the nucleation and propagation of α twins during deformation of Ti-6Al-4V.^[21]

The deformation modes that can be activated during deformation of LPBF Ti-6Al-4V is a complex issue. In addition to the microstructural features mentioned above, they depend on crystallographic texture, i.e. on the load direction.^[22-25] In this work, in situ high energy synchrotron X-ray diffraction (HEXRD) is carried out during compressive deformation to determine the sequence of activation of deformation mechanisms and its correspondence with the texture obtained in Ti-6Al-4V manufactured by LPBF. The deformation modes of LPBF Ti-6Al-4V are investigated for conditions deformed at 0°, 45° and 90° with respect to the LPBF building platform. The in situ time-resolved experiments using HEXRD allow for continuous tracking of the deformation mechanisms.

2. Experimental section

2.1. Laser powder bed fusion

LPBF of a Ti-6Al-4V (wt.%) grade 23 powder alloy was carried out in argon 5.0 atmosphere using a SLM280HL machine (SLM Solutions Group AG, Lübbeck, Germany). The temperature of the build platform was set to 200 °C. The powder alloy was produced by gas atomization and consisted of spherical particles of a size distribution $D_{10} = 22 \mu\text{m}$, $D_{50} = 34 \mu\text{m}$ and $D_{90} = 46 \mu\text{m}$, measured by the standard method ASTM B822. Cubic samples of $10 \times 10 \times 10 \text{ mm}^3$ were built using a chess scanning strategy. The laser pattern for the bulk material consists of chess domains, where the scanning vectors between these domains present a relative rotation of 90°.^[26] The LPBF processing parameters are summarized in **Table 1**. The volume energy density was calculated using **Equation 1**. The LPBF strategy aimed at applying an intensified intrinsic heat treatment (IHT) to promote decomposition of α'

martensite into stable α and β phases.^[7] This microstructure is sought to increase the ductility of Ti-6Al-4V.^[10,12,15]

For compression testing, LPBF cubic samples were machined into cylindrical specimens of 5.5 mm length and 3.5 mm diameter. In order to study the anisotropy of the alloy, the cylindrical samples were machined with the compression axis at 0°, 45° and 90° with respect to the base plate plane of the LPBF machine (hereinafter 0deg, 45deg and 90deg conditions, respectively). A schematic image of the compression directions of the samples with respect to the building platform is shown in **Figure 1**.

Table 1. LPBF parameters used for the processing of the samples.

Laser power P	Scanning velocity v	Hatch distance h	Focal offset distance F	Layer thickness d [μm]	Volume energy density E_v [J/mm ³]
[W]	[mm/s]	[μm]	[mm]		
250	1000	40	0	30	208

$$E_v = \frac{P}{v \cdot h \cdot d} \text{ [J/mm}^3\text{]} \quad (1)$$

Where E_v is the volume energy density; v is the scanning velocity; h is the hatch distance; and d is the layer thickness.

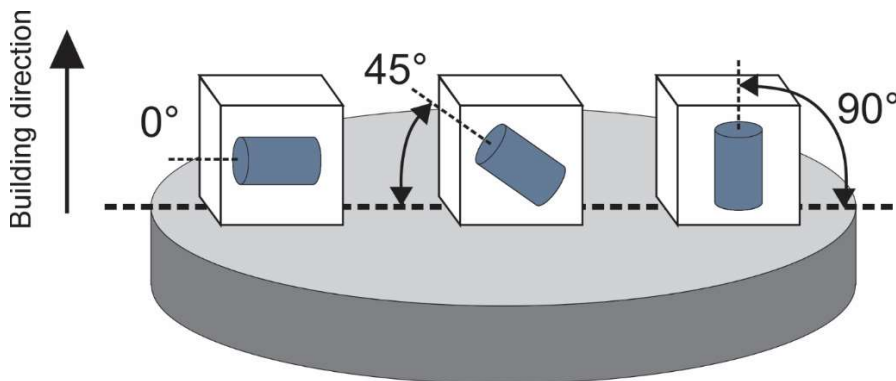


Figure 1. The samples investigated were manufactured in build directions of 0° (0deg), 45° (45deg) and 90°(90deg) with respect to the base plate of the LPBF machine.

2.2. In situ high energy synchrotron X-ray diffraction during uniaxial compression

In situ high energy synchrotron X-ray diffraction (HEXRD) during uniaxial compression was performed in transmission mode (sample thickness = 3.5 mm) at the beamline P07-HEMS of PETRA III (Deutsches Elektronen-Synchrotron, DESY, Hamburg, Germany).^[27] The energy of the X-ray beam and the wavelength used were 100 keV and 0.124 nm, respectively; the slit-aperture size of the beam 1×1 mm². The incident X-ray beam was positioned at the centre of the samples before and during deformation. A PerkinElmer XRD 1621 detector acquired the Debye-Scherrer rings during deformation at intervals of 0.5 s/image.

The compression tests were carried out at room temperature using a modified dilatometer Bähr 805A/D equipped with a deformation unit.^[28,29] The cylindrical samples were compressed at a strain rate of 0.002 s⁻¹. No buckling of the samples was observed during deformation. The effect of the dilatometer stiffness on the phase's macrostrains is assumed to be negligible. An illustrative diagram of the experimental setup is shown in **Figure 2a**.

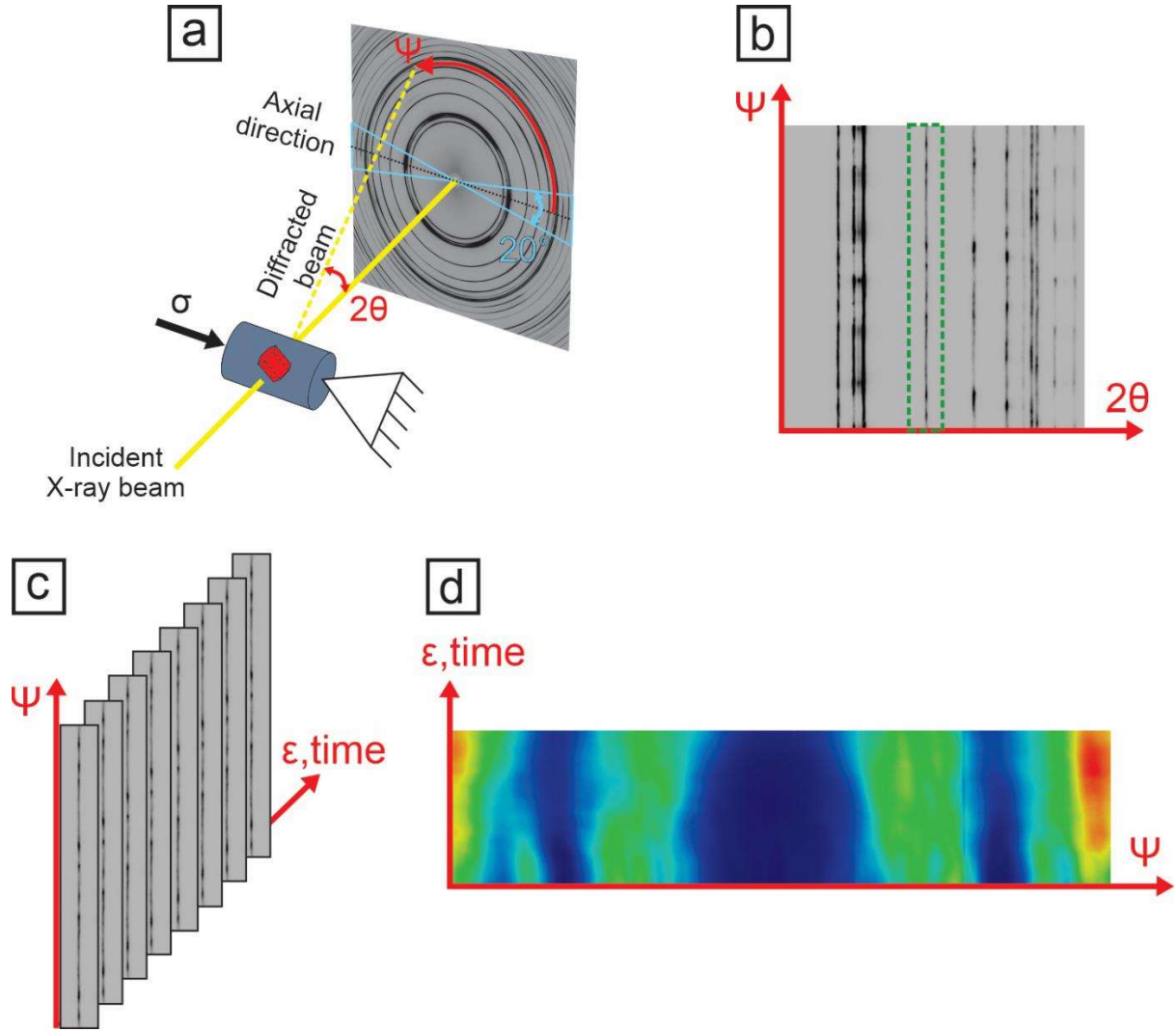


Figure 2. **a.** In situ high energy synchrotron X-ray diffraction during uniaxial compression: experimental setup. **b.** Debye–Scherrer rings unrolled and converted into Cartesian coordinates (Azimuthal angle ψ , 2θ). **c.** Example of the evolution as a function of strain for a single $\{h k l\}$ reflection shown in the selected inset (green dashed line) of Figure 2b. **d.** Normalized colour-coded 2D image corresponding to the evolution of a $\{h k l\}$ Bragg reflection intensity for the Azimuthal range 0-360° as a function of strain during uniaxial compression.

2.3. Data processing

In order to investigate the evolution of the diffraction images obtained in situ by HEXRD during deformation, the acquired Debye–Scherrer rings were unrolled and converted into

Cartesian coordinates (Azimuth angle ψ , 2θ), as shown in Figure 2b. Then, the unrolled $\{h k l\}$ reflexion was cut from the diffraction image, as indicated by the green dotted-line rectangle in Figure 2b. Using the software ImageJ, the intensity sum of Bragg reflections was projected on the $\psi - \varepsilon$ plane.^[30] This step is shown in Figure 2c. Finally, a normalized colour-coded 2D image is plotted, corresponding to the evolution of $\{h k l\}$ Bragg reflection intensity for the Azimuthal range 0-360° as a function of strain during uniaxial compression (Figure 2d).

The software Maud was employed for Rietveld and texture analyses of the diffraction patterns.^[31] An extended Williams-Imhof-Matthies-Vinel algorithm (E-WIMV) integrated in MAUD was used for texture analysis.^[31,32] The moment pole stress was employed as a stress model for the Rietveld refinement of the images acquired under compression.^[33,34] The instrumental parameters of the HEXRD setup were obtained from a LaB₆ powder standard. The Schmid factors of the α phase were calculated using the software MTEX and the crystal lattice parameters were obtained from Rietveld refinements.^[35]

Sections of 20° ($\pm 10^\circ$ with respect to the load) direction were taken from the Debye–Scherrer rings (Figure 2a) to calculate the lattice strains during deformation according to **Equation 2**.^[36] The 2θ variations of individual $\{h k l\}$ reflections in the load direction were considered for this analysis. Similarly, the calculation of the full width at half maximum (FWHM) were determined for cake portions of 20° in the load direction by single peak fitting (pseudo-Voigt approximation).

$$\varepsilon_{hkl} = \frac{d_{hkl} - d_{hkl}^0}{d_{hkl}^0} \quad (2)$$

where ε_{hkl} is the lattice strain of a $\{h k l\}$ plane family; d_{hkl}^0 and d_{hkl} are the plane spacings for the $\{h k l\}$ family before and during deformation, respectively.

2.4. Microstructure characterization

Scanning electron microscopy (SEM) in backscattered electron mode (BSE) was used to characterize the microstructure of the samples in the as-built condition. The SEM studies were performed employing a FEI Helios-Nanolab600i microscope (Thermofisher, Waltham, MA, USA). The specimens were prepared by grinding and polishing using a TegraPol machine with 3 μm diamond and SiO_2 suspension.

3. Results

Figure 3a and **b** show the initial microstructure of the LPBF as-built condition. Prior- β grain boundaries are highlighted by dashed lines in Figure 3a. Figure 3b shows that the microstructure is characterized by a partial decomposition of α' into $\alpha + \beta$. Layers of β can be observed in light grey (see arrows). The lamellar microstructure is composed of fine β layers decorating the $\alpha + \alpha'$ grains. These results correlate well with previous investigations reporting this effect using high energy density during LPBF.^[7,26] Regions with α and α' phases may be expected as a consequence of incomplete martensite decomposition. Since these similar hcp phases cannot be reliably distinguished using HEXRD, they will be referred to as α hereinafter.

Figure 3c shows the inverse pole figures of α for 0deg, 45deg and 90deg in the compression direction. In 0deg orientation, the maximum intensities are located close to the basal and prismatic planes. On the other hand, in the specimen at 45deg the maximum intensities are mainly found on the right side of the stereographic triangle, i.e. close to the $(10\bar{1}0)\alpha$ and $(2\bar{1}\bar{1}0)\alpha$ planes, as well as close to the basal plane. In contrast, for 90deg, the planes near $(2\bar{1}\bar{1}2)\alpha$ are those found most closely aligned to the load direction.

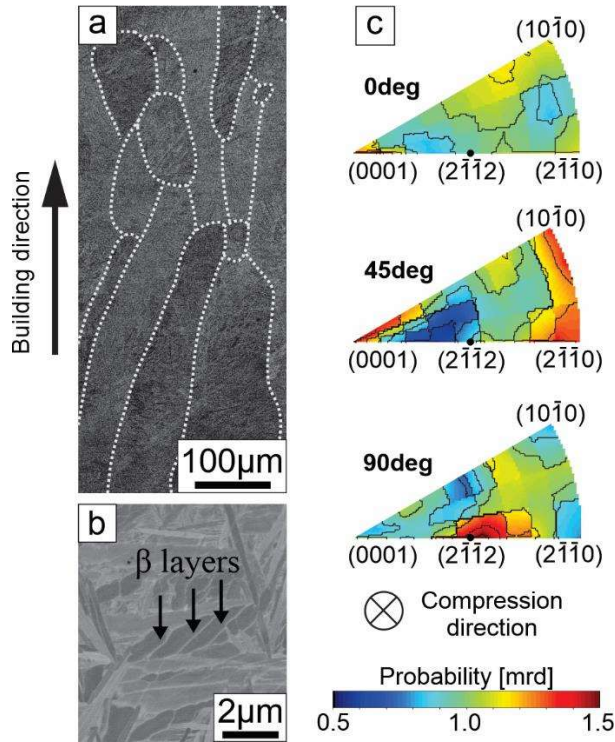


Figure 3. **a.** SEM-BSE image of the as-built LPBF condition. The prior- β grains are highlighted by dashed lines. **b.** SEM-BSE image with major magnification, where β layers are indicated by arrows. **c.** Inverse pole figures of α for 0deg, 45deg and 90deg orientations in the compression direction. The building direction is vertical for 0deg, 45° from the compression direction for 45deg and coincident with the compression direction for 90deg condition.

The true stress - strain curves obtained from the room temperature compression tests are plotted in **Figure 4a**. The 0deg orientation shows higher ductility and strength than the other two conditions. In order to analyse the work hardening behaviour of the three studied conditions, the evolution of the strain hardening rate (SHR) is shown as dot-line curves as a function of true strain (Figure 4a). It can be observed that the SHR for the 0deg condition is higher than for 45deg and 90deg during the entire deformation. Figure 4b shows the ultimate strength and deformation at break for the three studied orientations. The strength-ductility trade-off is maximum for 0deg. On the opposite, the 45deg condition presents the lowest ductility and strength.

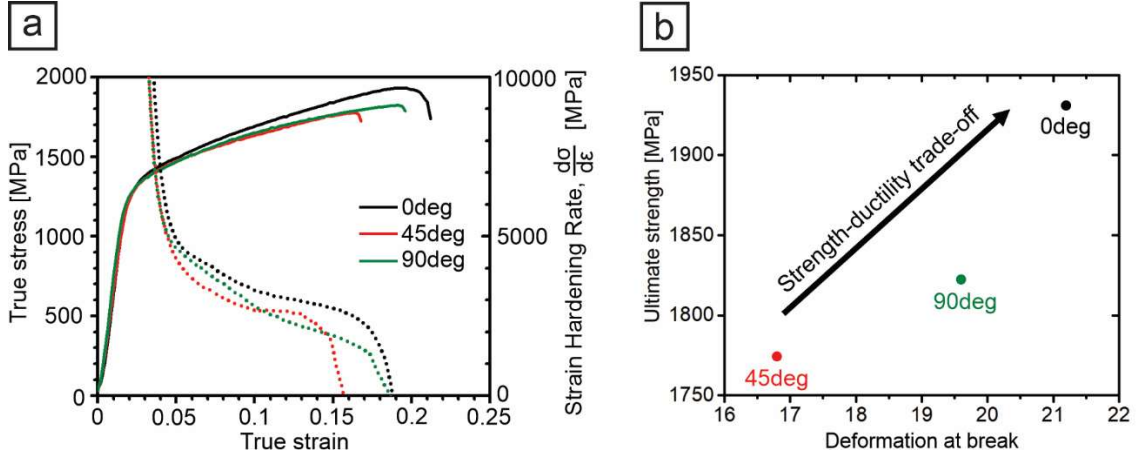


Figure 4. a. True stress – strain curves obtained during uniaxial compression. The strain hardening rate is also plotted as dot-line curves. **b.** Strength-ductility trade-off for the investigated conditions.

Fig. 5a-c show the evolution of the basal $\{0004\}\alpha$ reflections as a function of strain during compression for the 0deg, 45deg and 90deg conditions, respectively (Azimuthal range = 0-360°). The $\{0004\}\alpha$ reflection was chosen instead of $\{0002\}\alpha$ due to overlapping of the latter with the $\{110\}\beta$ reflection. The corresponding true stress – strain and SHR – true strain curves are also plotted on the right side of the 2D colour-coded plots. The horizontally built 0deg specimen (**Figure 5a**) shows reflections around $\psi \sim 15^\circ, 110^\circ, 195^\circ$ and 315° that begin to vanish at $\varepsilon \sim 0.05$. Simultaneously, new reflections become visible at $\psi \sim 40^\circ, 220^\circ$ and 260° . These sudden shifts are related to instantaneous rotations of a significant fraction of the crystals due to twinning.^[37] Some reflections ($\psi \sim 40^\circ$ and 220°) also show a continuous and slight shift of around 15° along the Azimuth angle, denoting the activation of slip-driven grain rotation as an acting plastic deformation mechanism.

In the 45deg condition, $\{0004\}\alpha$ reflections at $\psi \sim 110^\circ$ and 280° present continuous broadening as the strain increases (Figure 5b). This indicates that slip plays an important role as a plastic deformation mechanism in this condition. Also, the reflections at $\psi \sim 110^\circ$ and

280° present an increase in intensity at $\varepsilon \sim 0.05$, while those at $\psi \sim 0^\circ$ and 30° decrease their intensity. These effects are indications that strain-induced twinning may occur from $\varepsilon \sim 0.05$.

The 90deg condition presents a peak broadening which starts at $\varepsilon \sim 0.03$ up to the end of deformation in reflections at $\psi \sim 150^\circ$ and 330° (Figure 5c). In addition, at $\varepsilon \sim 0.05$ a sudden and remarkable intensity increase takes place in reflections located at $\psi \sim 55^\circ$ and 235° , and to a lesser extent at $\psi \sim 150^\circ$ and 330° . This suggests activation of twinning from this strain level.

Figures 5a-c indicate that both mechanisms of plastic deformation, namely slip and twinning, can be present in the three investigated conditions. However, the activation sequence and the mode that dominates the plastic deformation in each case seems to differ and is analysed below.

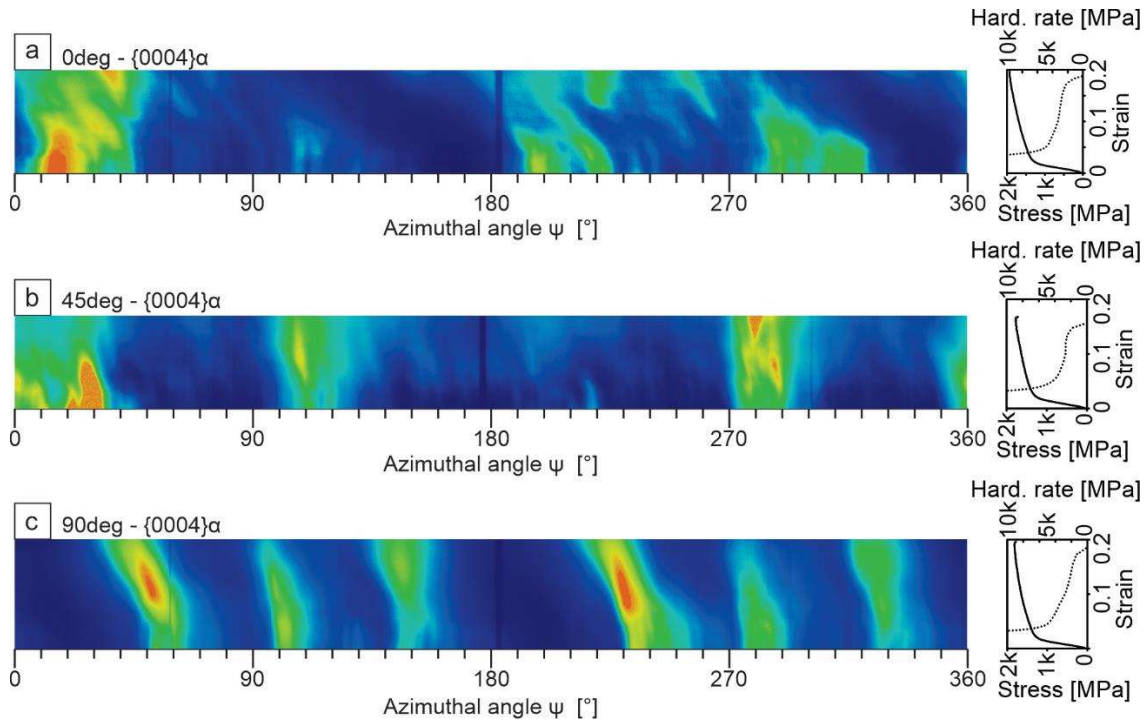


Figure 5. Colour-coded 2D plots corresponding to the evolution of $\{0004\}\alpha$ for the Azimuthal range 0–360° during uniaxial compression: **a.** 0deg; **b.** 45deg; **c.** 90deg. The true stress – strain and SHR – true strain curves are shown on the right side of the 2D plots.

The evolution of FWHM of the prismatic $\{01\bar{1}0\}\alpha$, basal $\{0002\}\alpha$ and pyramidal $\{01\bar{1}1\}\alpha$ planes is presented in Figure 6 to provide further insights of the mechanisms active during deformation. An increase of FWHM is generally related to peak broadening associated with the variation of type III microstrains provoked by lattice defects such as dislocations and stacking faults.^[38] In the 0deg orientation, the peak broadening gradually increases from $\varepsilon \sim 0.02$ as deformation progresses. This implies a continuous increase in the density of defects generated by slip in the α crystals. The basal plane undergoes the largest peak widening. In the 45deg condition, the peaks broaden in a similar manner as in the previous case, reaching a maximum at $\varepsilon \sim 0.12$, and then remaining constant until fracture. The broadening of $\{0002\}\alpha$ at the onset of plastic deformation is faster for the 90deg orientation than for the other conditions. The FWHM of this reflection reaches a maximum at $\varepsilon \sim 0.05$ and remains constant. On the other hand, the peak broadening of $\{01\bar{1}0\}\alpha$ and $\{01\bar{1}1\}\alpha$ undergo a lower increase until fracture.

The FWHM evolution shown in Figure 6 indicates different basal slip activities between orientations. While the 0deg condition exhibits a continuous slip activity throughout the experiment, the 45deg and 90deg orientations show a stepwise behaviour, i.e. the FWHM reaches a plateau. Moreover, in the 90deg condition, the alloy presents a very strong basal slip activity at the onset of plastic deformation. Thereafter, the FWHM of the basal plane remains relatively constant at $\varepsilon \sim 0.06$.

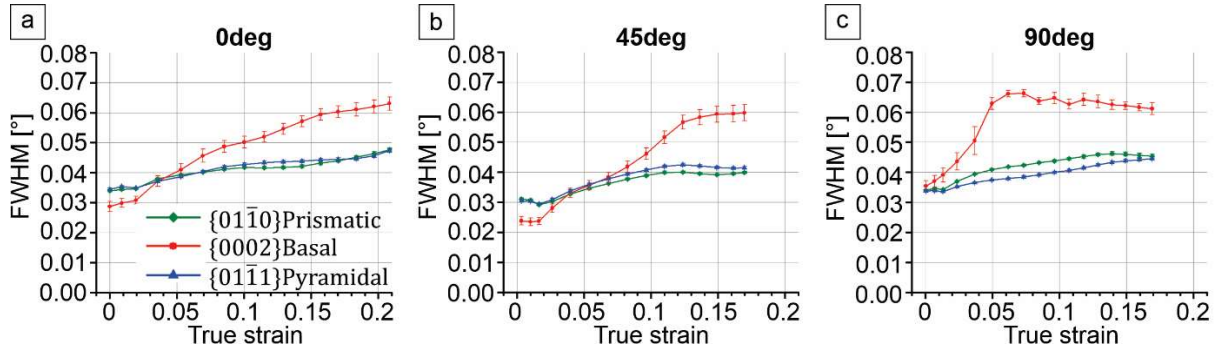


Figure 6. Evolution of FWHM along the compression direction for prismatic $\{01\bar{1}0\}\alpha$, basal $\{0002\}\alpha$ and pyramidal $\{01\bar{1}1\}\alpha$ planes during deformation for: **a.** 0deg; **b.** 45deg; and **c.** 90deg conditions.

It is expected that grains undergoing twin formation experience stress relaxation. Thus, the evolution of representative lattice strains of the α phase in the compression direction is plotted in **Figure 7** in order to identify the strain range during which twinning takes place. In the 0deg condition, a slight but continuous relaxation is observed in the plastic period at $\epsilon > 0.05$ for the prismatic and pyramidal planes. At $\epsilon > 0.19$, right before fracture, all planes experience an abrupt strain release. On the other hand, lattice relaxation was not observed in planes corresponding to 45deg orientation at any strain level. The 90deg condition presents an abrupt stress relaxation of the basal plane between $\epsilon \sim 0.05$ -0.10, which suggests a strong twinning formation in this stage of plastic deformation. From $\epsilon \sim 0.10$, the lattice strains of basal and prismatic planes undergo a slight increase until the sample fails.

These results correlate well with those shown in Figure 5a-c. In the 0deg condition, a combination of twinning and slip in α crystals takes place throughout the entire range of plastic deformation. Twinning-induced plasticity is revealed by sudden changes in intensity of some reflections (Figure 5a) and lattice strain relaxation (Figure 7a). On the other hand, slip is evidenced by the widening of the diffraction spots shown in Figure 5a and Figure 6a, and by

the inclination along the ψ axis of some reflections, which is an indication of grain rotation (Figure 5a).^[39]

The 90deg condition shows slip as the dominant mechanism at the onset of plastic deformation (Figures 5c and 6c). Twinning is then active from $\varepsilon \sim 0.05$ up to $\varepsilon \sim 0.10$: this can be deduced from the sudden intensity increase in reflections located at $\psi \sim 55^\circ$ and 235° in Figure 5c and from the lattice strain relaxation shown in Figure 7c.

In the 45deg orientation, slip is the main plastic deformation mode as evidenced by peak broadening, grain rotation, and the plateau of lattice strains shown in Figure 5-7. As a very minor contribution, twinning seems to be activated at approximately $\varepsilon > 0.05$, since some reflections suddenly change in intensity, as shown in Figure 5b.

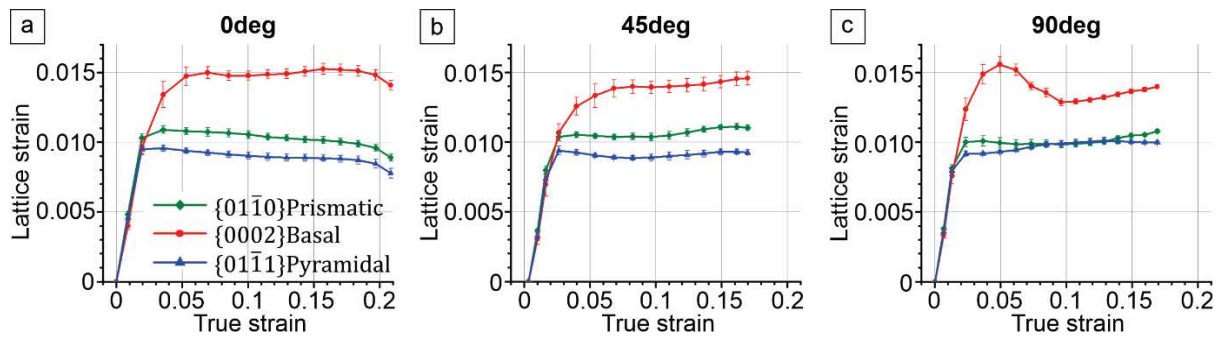


Figure 7. Evolution of lattice strains along the compression direction for prismatic $\{01\bar{1}0\}\alpha$, basal $\{0002\}\alpha$ and pyramidal $\{01\bar{1}1\}\alpha$ planes during deformation for: **a.** 0deg; **b.** 45deg; and **c.** 90deg conditions.

4. Discussion

4.1. Role of initial texture on deformation behaviour

The uniaxial compression tests performed for all conditions show that both slip and strain-induced twinning can be activated during deformation. However, the relevance and activation sequence of these mechanisms depends on the particular load direction and initial texture.

In the 0deg condition slip is activated at the onset of plastic deformation. This is evidenced by the increase in FWHM of the α reflections of basal, prismatic and pyramidal planes, shown in Figure 6a. At slightly higher strains (from $\varepsilon \sim 0.05$), twinning starts to assist slip, as shown by the sudden changes in intensity observed in Figure 5a. Similarly, in the 90deg condition the slip activity that occurs from the onset of the plastic deformation coexists with twinning, mainly between $\varepsilon \sim 0.05$ and $\varepsilon \sim 0.10$, as it was shown in Figures 5c, 6c and 7c. The trigger for the initiation of twinning may be the hardening that occurs in the alloy due to the increasing of dislocation density by slip, which is also related to an increment in the critical resolved shear stress (CRSS).^[40] This can cause some grains to become prone to twinning when the CRSS of the slip system that dominated the plastic deformation up to that point reaches a critical value. On the other hand, in the 45deg condition, it can be assumed that slip is the dominant mechanism since a continuous increase of FWHM is observed (Figure 6b) and the twinning indications are weaker than in 0deg and 90deg conditions (no relaxation of lattice strains, Figure 7b, and low activity of intensity changes, Figure 5b).

The Schmid's law establishes a geometrical criterion to evaluate the inclination of crystallographic systems to deform via slip and twinning. This law is generally used for single crystals under uniaxial load and for slip as deformation mechanism. However, it can also be used to evaluate qualitatively the tendency of the grains to deform by a particular deformation mode.^[41] **Figure 8a** and **b** shows the Schmid factors (SF) as a function of the crystallographic orientation for basal, prismatic and pyramidal slip systems, and for the main types of deformation twinning systems that can occur in α titanium.^[42] Each one of these twinning modes is associated with a particular axis (r) and angle of rotation (ω). The latter represents the misorientation between the parent grain and the twin. While tensile twinning introduces a positive strain along the c-axis of the parent α grain, compression twinning implies a negative component of strain along the c-axis.^[43] Tensile twins are often found in specific microstructural areas of a material subjected to compression when a crystal has the c-axis

oriented perpendicular to the compression axis, and its extension is therefore required to accommodate deformation. The directional dependence of twinning for hcp crystals can be observed in the SF corresponding to twinning systems in Figure 8b. The compression twinning system presents maximum SF when the compression direction is perpendicular to the basal plane, and decreases as the c-axis moves away from the load direction. In contrast, the SF of tensile twinning systems has a maximum when the c-axis is perpendicular to the compression direction. It should be noted that the CRSS for the basal and prismatic slip systems in Ti–6Al–4V are very similar to each other, and they are much lower than that for the pyramidal system.^[44] This implies that for a grain with a high SF for the pyramidal slip system, the other two slip systems can be activated first because their CRSS is smaller.

By comparing the initial texture presented in the IPF of Figure 8c with the SF in Figure 8a-b, the 0deg orientation presents a texture with the majority of the grains prone to activate several deformation systems: $\{11\bar{2}2\}\alpha$ compression and $\{11\bar{2}1\}\alpha$ tensile twinning as well as prismatic and pyramidal slip. This texture distribution with favourably-oriented grains for twinning or slip activation explains the mechanical behaviour of this condition at beginning of the compression test. The initial orientation of grains in this condition, prone to trigger both tensile and compression twinning modes, indicates that both processes may take place during deformation. This agrees with Figure 5a, where several sudden intensity changes can be seen for this condition, although it is not possible to identify a defined angle of rotation. This could indicate that more than one twinning system is activated. It is also possible that these twinning systems are being activated sequentially, as it is widely reported for pure Ti and α -Ti alloys.^[42,44-47]

The initial texture in the 45deg orientation is very favourable for activating the prismatic slip system, as it can be observed in the IPF shown in Figure 8c. Although some grains are well oriented to activate $\{11\bar{2}2\}\alpha$ compression and $\{11\bar{2}1\}\alpha$ tensile twinning systems, the

prismatic slip system is associated with a low CRSS. Thus, it is plausible that the latter dominates over the twinning deformation modes.^[44]

The deformation mechanisms that can be activated at the beginning of compression for the 90deg condition are slip in the basal system as well as pyramidal slip and $\{11\bar{2}1\}\alpha$ tensile twinning, as observed by comparing Figure 8a, b and c. The initial texture, strongly oriented close to the $\{2\bar{1}\bar{1}2\}$ plane, indicates that the initial deformation mechanism that governs at the onset of plastic range is slip in the basal plane system. This can be seen in the rapid broadening of the $\{0002\}\alpha$ reflection during the initial stage of plastic deformation, as it was shown in Figure 6. The grains favourably-oriented for $\{11\bar{2}1\}\alpha$ tensile twinning may be responsible for the strain-induced twinning activity, higher than in the 45deg condition but lower than in the 0deg condition, as it was shown in Figures 5-7. Compression twinning is initially restricted in this condition because there are not many grains with the c-axis oriented in the load direction at the beginning of compression.

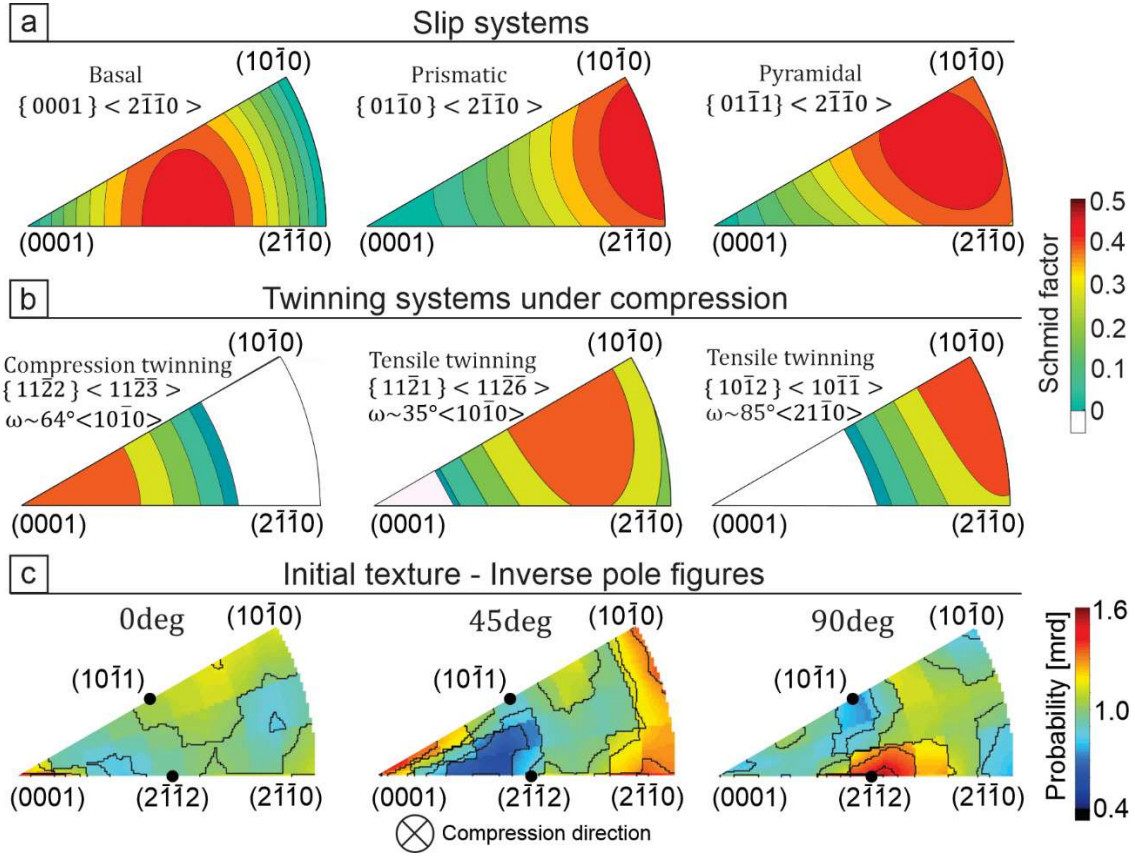


Figure 8. Schmid factors as a function of crystallographic orientation for: **a.** basal, prismatic and pyramidal slip systems; **b.** $\{11\bar{2}2\}\alpha$, $\{11\bar{2}1\}\alpha$ and $\{10\bar{1}2\}\alpha$ twinning systems under compression. **c.** Inverse pole figures of α showing the initial texture for the three investigated conditions.

4.2. Texture evolution during compression

A sequential texture development is generally observed in materials where twinning makes a major contribution to plastic deformation.^[47] This is related to the reorientation of domains within grains during the nucleation and growth of twins. As can be seen in Figure 5a, the 0deg condition seems to show the most remarkable texture variation. The IPF at different strain levels are shown in **Figure 9a** to better understand the evolution of texture during compression. The texture changes considerably during deformation in the 0deg orientation. The most remarkable variation is the decrease in intensity near the direction of the $\{10\bar{1}0\}\alpha$

plane. These orientations have high SF for both tensile twinning modes, $\{11\bar{2}1\}\alpha$ and $\{10\bar{1}2\}\alpha$, as it was shown in Figure 8. This is associated with the intensity increase at the base of stereographic triangle, between $\{2\bar{1}\bar{1}2\}\alpha$ and $\{2\bar{1}\bar{1}0\}\alpha$, as indicated by the arrow in Figure 9a. This figure shows that this increment in intensity can be related to the activation of $\{11\bar{2}1\}\alpha$ tensile twinning in crystals oriented near $\{10\bar{1}0\}\alpha$, with a shift of about 35° and $\langle 2\bar{1}\bar{1}0 \rangle$ as the rotation axis. The calculated angle of rotation ω is 34° , very close to the theoretical angle, and the axis of rotation r is $\langle 2.9 \ 1.7 \ 1.2 \ 0.5 \rangle$, only 8° away from the $\langle 2\bar{1}\bar{1}0 \rangle$ theoretical axis. Although a slight increase in intensity can be observed near the $\{10\bar{1}1\}\alpha$ orientation at $\varepsilon = 0.11$, no rotations compatible with twinning systems were found for this reflection. This may be due to a sequential combination of different twinning systems, which modifies the rotation of the twin with respect to the matrix.^[42] The stress-strain curve for this condition shows a strength-ductility trade-off higher than the other two orientations. We suggest that this is related to the combined activation of slip and strain-induced twinning, which also produces a high strain hardening rate.

Less significant texture changes than in the previous case were observed in the 45deg condition (Figure 9b). This is compatible with slip as the dominant mode of plastic deformation. A slight increase in intensity near $\{2\bar{1}\bar{1}2\}\alpha$ orientation is compatible with the formation of $\{11\bar{2}1\}\alpha$ tensile twinning in grains oriented close to $\{10\bar{1}0\}\alpha$. The rotation between parent and twin is represented by an angle of rotation ω of 42° (7° away from the theoretical one) and an axis of rotation $r \langle 2.9 \ 1.5 \ 1.4 \ 0.1 \rangle$ (1.5° of difference with the $\langle 2\bar{1}\bar{1}0 \rangle$ theoretical axis). In the 45deg condition, the tendency to activate the prismatic slip system in detriment of the other deformation modes, fundamentally the twinning systems, seems responsible for the low elongation at break and SHR achieved.

The initial texture of the 90deg condition, with most of the grains oriented far from the $\{0001\}\alpha$ basal plane, restricts the activation of compression twinning (Figure 9c). However,

many crystals are prone to activate basal slip and $\{11\bar{2}1\}\alpha$ tensile twinning. These two mechanisms govern plastic deformation in this condition. Similar rotations to those shown in the two previous cases were found. These are compatible with $\{11\bar{2}1\}\alpha$ tensile twinning in grains oriented close to $\{10\bar{1}0\}\alpha$ orientation. The texture evolution has similarities to that observed in Figure 9a for the 0deg condition: an intensity decrease can be observed close to the $\{10\bar{1}0\}\alpha$ plane, i.e. a region that corresponds to a high SF for $\{11\bar{2}1\}\alpha$ tensile twinning (Figure 8b). The 90deg condition shows a lower amount of domains oriented close to the $\{10\bar{1}0\}\alpha$ plane than the 0deg condition (compare the IPF in Fig. 10a and c). Therefore, a lower strain-induced twinning activity can be expected for the 90deg condition, which may be responsible for the higher strength-ductility trade-off of 0deg.

Despite the fact that the three studied conditions present an initial texture with grains prone to activate the two tensile twinning systems, only $\{11\bar{2}1\}\alpha$ twinning seems to be active during compression. In pure Ti, the governing twinning mode is $\{10\bar{1}2\}$.^[42] However, as the content of Al increases, this deformation mechanism is abruptly restricted.^[48] This was attributed to a higher stacking fault energy and yield stress with increasing Al.^[48] In this sense, the 6 wt% of Al in Ti-6Al-4V may be responsible for the difference in the activation of twinning mechanisms compared to pure Ti.

For pure Ti, it is commonly known that twinning plays a fundamental role during plastic deformation. However, there are limited reports of twinning in Ti-6Al-4V.^[21-22,49,50] This study points to twinning as an important deformation mode for this alloy when produced by LPBF. In this sense, a favourable initial texture is fundamental for the activation and propagation of $\{11\bar{2}1\}\alpha$ tensile twinning.

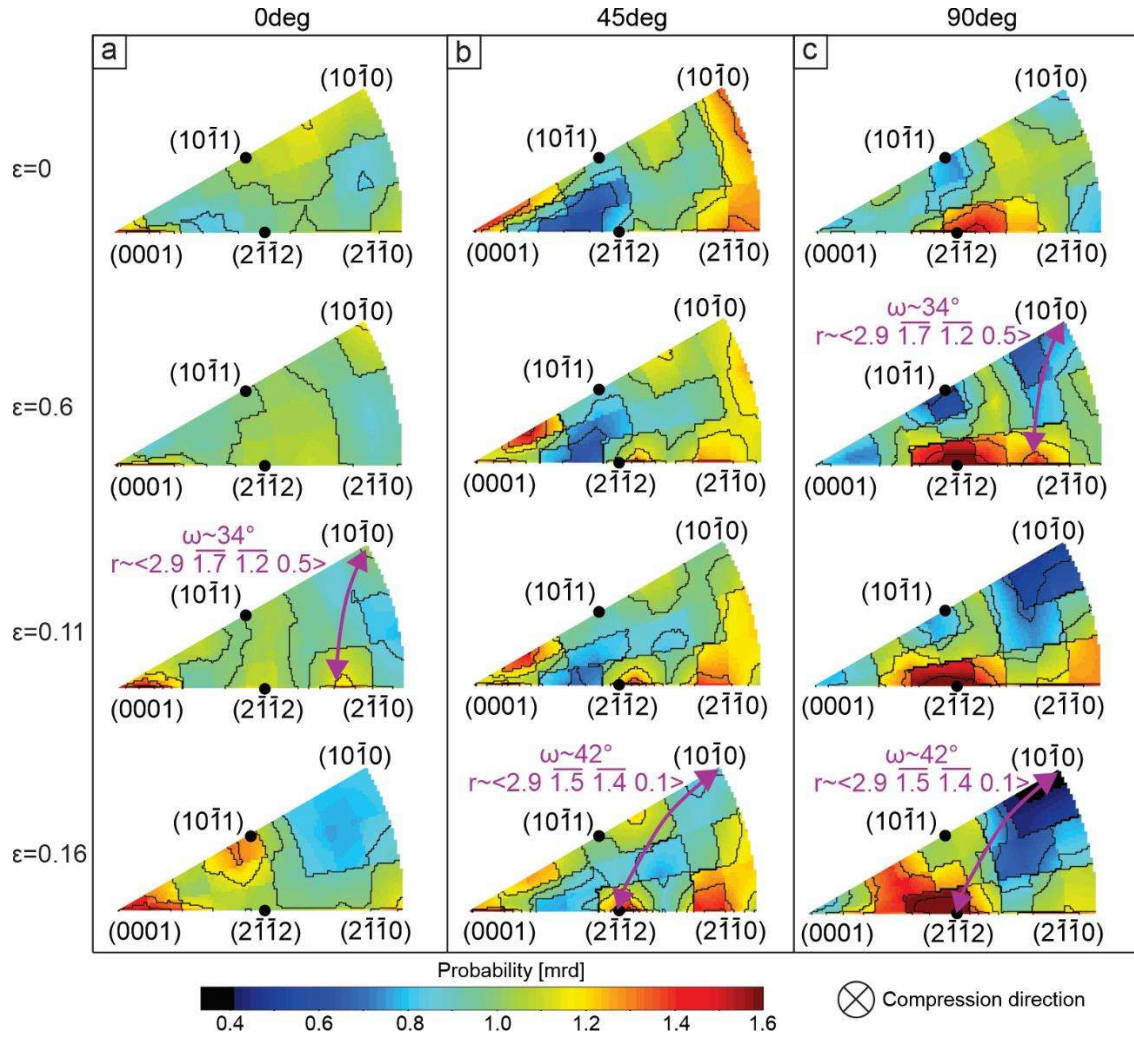


Figure 9. Inverse pole figures at representative strain levels showing the texture evolution during uniaxial compression for: **a.** 0deg; **b.** 45deg; **c.** 90deg conditions.

As a summary, **Figure 10a-c** shows the dominant deformation mechanisms observed for each deformation stage in the 0deg, 45deg and 90deg conditions, respectively. For the 0deg orientation, a combination of three mechanisms govern the plastic deformation: basal and prismatic slip and $\{11\bar{2}2\}\alpha$ tensile twinning. The relatively larger amount of domains oriented close to $\{10\bar{1}0\}\alpha$ compared to the 90deg condition and the coexistence of the three deformation modes throughout the entire range of plastic deformation makes it possible to achieve a higher strength ductility trade-off in this condition. Moreover, the occurrence of more than one twinning mode in a sequential and combined way in the 0deg orientation is

possible because not all rotations were identified with a particular twinning system.^[42] Despite the fact that this condition presents favourable grains to activate compression twinning, this mode of deformation could not be clearly observed in Figure 9a. Therefore, it is not included in Figure 10a as a dominant mechanism of deformation, although it could assist in the plastic deformation of the alloy in this orientation. On the other hand, slip in the basal system dominates the initial plastic deformation in the 90deg orientation, followed by a combination of slip and $\{11\bar{2}1\}\alpha$ tensile twinning, fundamentally in $\epsilon \sim 0.05-0.1$. Basal slip is considered to be the dominant mechanism in the second stage of deformation, while twinning assists it to accommodate compression deformation. This assumption is based on the fact that this condition showed less signs of twinning than in the previous case and that the initial texture is well oriented to activate slip in the basal plane. In this condition, a deformation at break of $\epsilon \sim 0.2$ is reached. The mechanism that dominates the plastic deformation in the 45deg orientation is slip in the α prismatic system. Twinning plays a secondary role and as a consequence, the deformation at break and the ultimate strength are lower than in the previous cases.

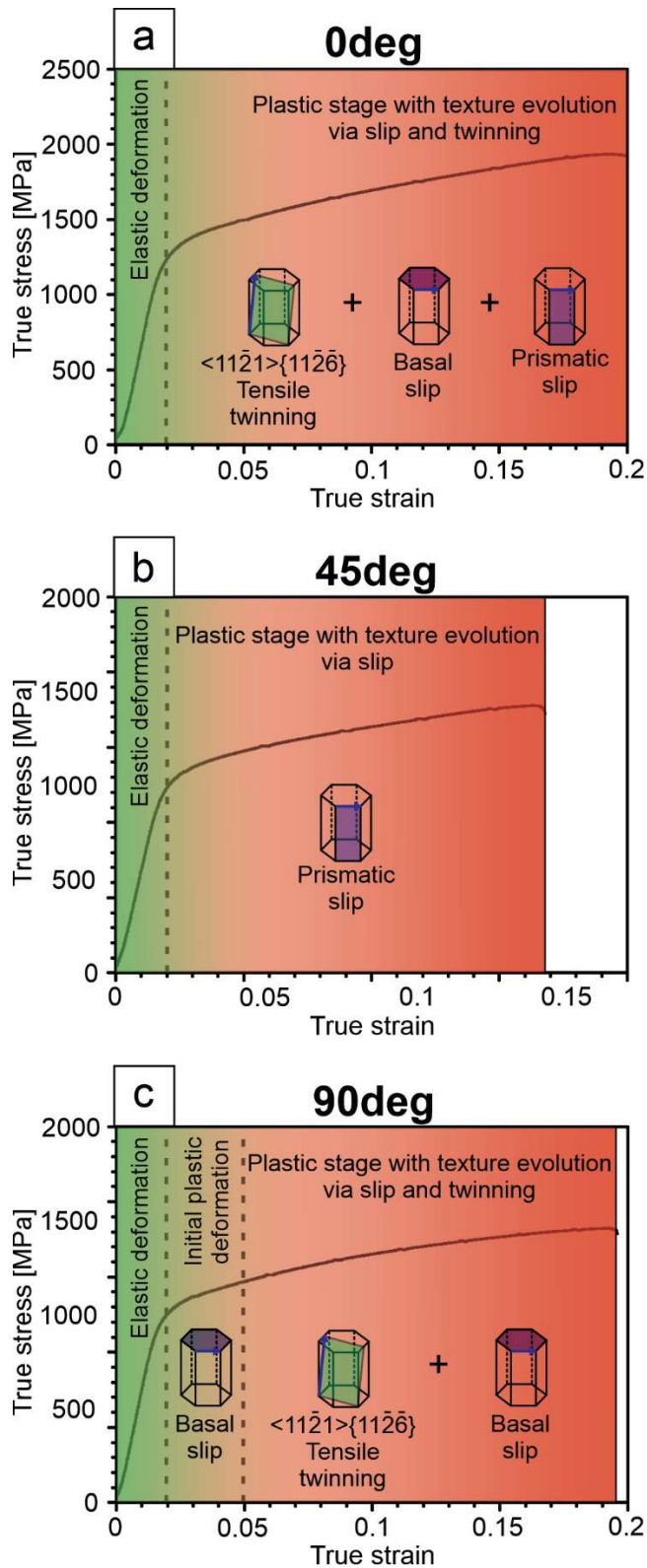


Figure 10. Plastic deformation mechanisms dominating in each deformation stage indicated on the true stress- strain curves of: **a.** 0deg; **b.** 45deg; **c.** 90deg conditions.

5. Conclusions

In this work, the deformation mechanisms under compression of Ti-6Al-4V processed by laser powder bed fusion (LPBF) were investigated in situ using high energy synchrotron X-ray diffraction (HEXRD). To this purpose, samples oriented at 0°, 45° and 90° with respect to the LPBF build plate were investigated. These are three conditions with different initial textures of the α phase with respect to the load direction. In situ compression tests were performed during HEXRD to monitor the evolution of the microstructure during deformation.

The following conclusions can be drawn:

- A microstructure derived from the partial decomposition of α' into α grains and β layers was obtained within prior β grains by LPBF as a consequence of the intensified intrinsic heat treatment applied during LPBF. The prior β grains have predominantly columnar shapes, while some globular grains were also observed.
- The highest ultimate strength and deformation at break was obtained in the 0deg condition. On the contrary, the lower strength-ductility trade-off was observed for the 45deg condition. The higher deformation at break obtained in the 0deg and 90deg conditions is a consequence of the substantial contribution of $\{11\bar{2}1\}\alpha$ tensile twinning to the plastic deformation of the alloy.
- The initial texture plays an important role in the resulting strength-ductility trade-off. An initial texture favourable for $\{11\bar{2}1\}\alpha$ tensile twinning, with several grains oriented near $\{10\bar{1}0\}\alpha$ orientation, produces a sequential and synergistic activation of slip and twinning deformation modes that lead to an improved mechanical response. On the other hand, an initial texture for which prismatic slip dominates deformation, with grains oriented near $\{10\bar{1}0\}\alpha$ and $\{2\bar{1}\bar{1}0\}\alpha$ orientations, restricts the mechanical performance of LPBF Ti-6Al-4V.
- A fast evolution of texture was observed in the conditions where twinning produced a substantial contribution to plastic deformation, i.e. 0deg and 90 deg. The texture

evolution in this conditions shows sudden grain rotations, compatible with $\{11\bar{2}1\}\alpha$ tensile twinning. On the other hand, the texture during compression in the 45deg build orientation show minor changes, as expected from a condition in which slip in prismatic system dominates plastic deformation. Also, the rotations in this condition are compatible with $\{11\bar{2}1\}\alpha$ tensile twinning.

The results obtained in this work show that there are still windows of opportunity to adjust the strength-ductility trade-off of LPBF Ti-6Al-4V by tuning initial texture and exploiting the combined effects of slip and twinning.

Acknowledgements

The Deutsches Elektronen-Synchrotron (DESY) is acknowledged for the provision of synchrotron radiation facilities in the framework of the proposal I-20191042.

References

- [1] C. Leyens, M. Peters, *Titanium and Titanium Alloys: Fundamentals and Applications*, Wiley-VCH, Weinheim, Germany **2003**.
- [2] C. Cui, B. Hu, L. Zhao, S. Liu, *Materials & Design* **2011**, 32, 1684.
- [3] G. Lütjering, *Mater. Sci. Eng. A* **1998**, 243, 32.
- [4] G. Lütjering, J.C. Williams, *Titanium*, Springer, New York, USA **2007**.
- [5] R. Huang, M. Riddle, D. Graziano, J. Warren, S. Das, S. Nimbalkar, J. Cresko, E. Masanet, *Journal of Cleaner Production* **2016**, 135, 1559.
- [6] T. Vilaro, C. Colin, J.D. Bartout, *Met. Mat. Trans. A Phys. Metallurgy* **2011**, 42A, 3190.
- [7] P. Barriobero-Vila, J. Gussone, J. Haubrich, S. Sandlöbes, J. Da Silva, P. Cloetens, N. Schell, G. Requena, *Materials* **2017**, 10, 268.

- [8] S.Q. Wu, Y.J. Lu, Y.L. Gan, T.T. Huang, C.Q. Zhao, J.J. Lin, S. Guo, J.X. Lin, *J. Alloy. Comp.* **2016**, 672, 643.
- [9] G. Kasperovich, J. Haubrich, J. Gussone, G. Requena, *Mat. & Des.* **2016**, 105, 160.
- [10] W. Xu, M. Brandt, S. Sun, J. Elambasseril, Q. Liu, K. Latham, K. Xia, M. Qian, *Acta Mater.* **2015**, 85, 74.
- [11] J.J. Yang, H.C. Yu, J. Yin, M. Gao, Z.M. Wang, X.Y. Zeng, *Mat. & Des.* **2016**, 108, 308.
- [12] W. Xu, E.W. Lui, A. Pateras, M. Qian, M. Brandt, *Acta Mater.* **2017**, 125, 390.
- [13] J.J. Yang, J. Han, H.C. Yu, J. Yin, M. Gao, Z.M. Wang, X.Y. Zeng, *Mat. & Des.* **2016**, 110, 558.
- [14] X.Y. Zhang, G. Fang, S. Leeftang, A.J. Bottger, A.A. Zadpoor, J. Zhou, *J. Alloy. Comp.* **2018**, 735, 1562.
- [15] D. Agius, K.I. Kourousis, C. Wallbrink, *Metals* **2008**, 8, 75.
- [16] C. De Formanoir, S. Michotte, O. Rigo, L. Germain, S. Godet, *Mater. Sci. Eng. A* **2016**, 652, 105.
- [17] V. Popov, A. Katz-Demyanetz, A. Garkun, G. Muller, E. Strokin, H. Rosenson, *Procedia Manuf.* **2018**, 21, 125.
- [18] J. Haubrich, J. Gussone, P. Barriobero-Vila, P. Kürnsteiner, E. Jäggle, D. Raabe, N. Schell, G. Requena, *Acta Mater.* **2019**, 167, 136.
- [19] H. Matsumoto, H. Yoneda, K. Sato, S. Kurosu, E. Maire, D. Fabregue, T.J. Konno, A. Chiba, *Mater. Sci. Eng. A* **2011**, 528, 1512.
- [20] A. Zafari, K. Xia, *Materials Research Letters* **2018**, 6 (2018), 627.
- [21] X. Zheng, S. Zheng, J. Wang, Y. Ma, H. Wang, Y. Zhou, X. Shao, B. Zhang, J. Lei, R. Yang, X. Ma, *Acta Mater.* **2019**, 181, 479.
- [22] A.W. Bowen, *Materials Science and Engineering* **1979**, 40, 31.
- [23] M. Simonelli, Y.Y. Tse, C. Tuck, *Materials Science & Engineering A* 2014, 616, 1.

- [24] F. Wang, S. Williams, P. Colegrove, A. Antonysamy, *Metallurgical and Materials Transactions A* **2013**, 44, 968.
- [25] T. Scharowsky, V. Juechter, R. Singer, C. Körner, *Advanced Engineering Materials* **2015**, 17, 1573.
- [26] P. Barriobero-Vila, K. Artzt, A. Stark, N. Schell, M. Siggel, J. Gussone, J. Kleinert, W. Kitsche, G. Requena, J. Haubrich, *Scripta Mater.* **2020**, 182, 48.
- [27] N. Schell, A. King, F. Beckmann, T. Fischer, M. Müller, A. Schreyer, *Mater. Sci. Forum* **2014**, 772, 57.
- [28] P. Staron, T. Fischer, T. Lippmann, A. Stark, S. Daneshpour, D. Schnubel, E. Uhlmann, R. Gerstenberger, B. Camin, W. Reimers, E. Eidenberger, H. Clemens, N. Huber, A. Schreyer, *Adv. Eng. Mater.* **2011**, 13, 658.
- [29] P. Barriobero-Vila, J. Gussone, K. Kelm, J. Haubrich, A. Stark, N. Schell, G. Requena, *Mater. Sci. Eng. A* **2018**, 717, 134.
- [30] C.A. Schneider, W.S. Rasband, K.W. Eliceiri, *Nature methods* **2012**, 9, 671.
- [31] L. Lutterotti, S. Matthies, H. R. Wenk, A. J. Schultz, J. Richardson, *J. Appl. Phys.* **1997**, 81, 594.
- [32] L. Lutterotti, D. Chateigner, S. Ferrari, J. Ricote, *Thin Solid Films* **2004**, 450, 34.
- [33] S. Matthies, S., *Textures Microstructures* **1996**, 25, 229.
- [34] S. Matthies, H.G. Priesmeyer, M.R. Daymond, *Journal of Applied Crystallography* **2001**, 34, 585.
- [35] R. Hielscher, H. Schaeben, *J. Appl. Cryst.* **2008**, 41, 1024.
- [36] O. Muránsky, D.G. Carr, M.R. Barnett, E.C. Oliver, P. Sittner, *Mater. Sci. Eng. A* **2008**, 496, 14.
- [37] K. Yan, D.G. Carr, M.D. Callaghan, K-D Liss, H. Lia, *Scripta Mater.* **2010**, 62, 246.
- [38] R.L. Rothman, J.B. Cohen, *Journal of Applied Physics* **1971**, 42, 971.

- [39] D. Canelo-Yubero, C. Poletti, F. Warchomicka, J. Daniels, G. Requena, *Journal of Alloys and Compounds* **2018**, 764, 937.
- [40] B. Clausen, C.N. Tomé, D.W. Brown, S.R. Agnew, *Acta Materialia* **2008**, 56, 2456.
- [41] E. Schmid, W. Boas, *Kristallplastizität: Mit Besonderer Berücksichtigung der Metalle*, Springer, Berlin, Germany **1935**.
- [42] N. Bozzolo, L. Chan, A.D. Rollett, *J. Appl. Cryst.* **2010**, 43, 596.
- [43] X. Liao, J. Wang, J. Nie, Y. Jiang, P. Wu, *MRS Bulletin* **2016**, 41, 314.
- [44] F. Bridier, P. Villechaise, J. Mendez, *Acta Materialia* **2005**, 53, 555.
- [45] W. Tirry, M. Nixon, O. Cazacu, F. Coghe, L. Rabet, *Scr. Mater.* **2011**, 64, 840.
- [46] S. Xu, L.S. Toth, C. Schuman, J.-S. Lecomte, M.R. Barnett, *Acta Materialia* **2017**, 124, 59.
- [47] S. Xu, M. Gong, C. Schuman, J.-S. Lecomte, X. Xie, J. Wang, *Acta Materialia* **2017**, 132, 57.
- [48] A. Fitzner, D.G.L. Prakash, J.Q. da Fonseca, M. Thomas, S.-Y. Zhang, J. Kelleher, P. Manuel, M. Preuss, *Acta Materialia* **2016**, 103, 341.
- [49] D.G. Leo Prakash, R. Ding, R.J. Moat, I. Jones, P.J. Withers, J. Quinta da Fonseca, M. Preuss, *Materials Science and Engineering A* **2010**, 527, 5734.
- [50] H.Z. Zhong, X.Y. Zhang, S.X. Wang, J.F. Gu, *Materials and Design* **2018**, 144, 14.